Plasmodium falciparum disruption of pericyte angiopoietin-1 secretion contributes to barrier breakdown in a 3D brain microvessel model

Rory K. M. Long[1,2], François Korbmacher[1], Paolo Ronchi[3], Hannah Fleckenstein[1,3], Waleed Mirza[1], Mireia Mallorquí[1], Ruth Aguilar[4], Gemma Moncunill[4], Yannick Schwab[3], Maria Bernabeu[1*]

[1]*European Molecular Biology Laboratory (EMBL) Barcelona, Barcelona, Spain*
[2]*Heidelberg University, Faculty of Biosciences, Heidelberg, Germany*
[3]*European Molecular Biology Laboratory (EMBL), Cell Biology and Biophysics Unit, Heidelberg, Germany.*
[4]*Barcelona Institute for Global Health (ISGlobal), Hospital Clínic-Universitat de Barcelona, Barcelona, Spain*

*To whom correspondence should be addressed. Email: maria.bernabeu@embl.es

Abstract:
Disruption of the angiopoietin-Tie axis is a common finding in cerebral malaria (CM) patients. Increased concentrations of angiopoietin-2 (Ang-2) and decreased levels of angiopoietin-1 (Ang-1) correlate with disease severity and have been proposed as biomarkers of CM. Brain pericytes have a key role in promoting vascular quiescence through many pathways, including Ang-1 secretion. Despite evidence of pericyte damage on post-mortem samples of CM patients, their role in the pathogenesis of the disease remains unexplored. To address this question, we engineered a 3D microfluidics-based cerebral microvessel model containing both human primary cerebral microvascular endothelial cells and cerebral vascular pericytes. This model replicated pericyte vessel coverage and ultrastructural endothelial-pericyte interactions present in the *in vivo* brain microvascular bed. 3D brain microvessels experienced an increase in vascular permeability after exposure to purified *P. falciparum*-iRBC egress products. This was accompanied by minor changes in pericyte ultrastructural morphology detected by serial block-face scanning electron microscopy. Luminex quantification of cytokines secreted by bioengineered microvessels revealed a significant decrease in Ang-1 secretion and increase in the Ang-2/Ang-1 ratio, suggesting that *P. falciparum*-iRBC egress products directly disrupt pericyte biology. Furthermore, we show that pre-incubation with recombinant Ang-1 partially protects against microvessel barrier breakdown caused by *P. falciparum*-iRBC egress products. Our approach

highlights a novel role of brain pericytes in CM pathogenesis and indicates that dysregulation in the angiopoietin-Tie axis contributes to *P. falciparum*-mediated vascular dysfunction.

Significance:

Cerebral malaria is caused by brain endothelial disruption mediated by *Plasmodium falciparum* infection. However, the contribution of other brain vascular cell types in disease pathogenesis remains unexplored. Here, we created an *in vitro* model of the brain microvasculature comprised of brain endothelial cells and pericytes, a cell type that supports vascular quiescence. We found that barrier disruptive products released from *Plasmodium falciparum*-infected red blood cells trigger minor pericyte morphological changes and inhibit the secretion of angiopoietin-1, a key barrier protective endothelial ligand. The external addition of angiopoietin-1 into the model partially restored microvascular barrier function after exposure to *P. falciparum* egress products, highlighting the role of brain pericytes in cerebral malaria formation and suggesting future therapeutic avenues.

Introduction:

Cerebral malaria (CM) is a severe neurological complication of *Plasmodium falciparum* infection, clinically characterized by coma and fatality rates averaging 15-20% (1). Furthermore, approximately 20% of CM survivors endure lifelong neurological sequelae such as hemiplegia, ataxia, epilepsy or speech disorders (2). The majority of pediatric CM-related deaths present severe brain swelling due to vasogenic edema, likely as a consequence of blood-brain barrier dysfunction (3). A hallmark of CM is the sequestration of *P. falciparum*-infected red blood cells (iRBC) in the brain microvasculature (4). While the molecular players responsible for *P. falciparum*-iRBC ligand-receptor interactions with cerebral endothelial cells have been extensively studied (5–7), the consequences of iRBC sequestration to the brain microvasculature require further investigation. Nevertheless, evidence suggests that the increase in vascular permeability is a result of a multifaceted process including a blockade of barrier-supportive endothelial receptors by iRBC, the release of toxic *P. falciparum* products from egressed iRBC, and a dysregulated host innate immune response (8, 9).

An important pathway commonly dysregulated in CM patients is the angiopoietin-Tie axis, crucial to maintaining endothelial pro-barrier, anti-inflammatory, and anti-apoptotic functions (10). Binding of the vascular ligand angiopoietin-1 (Ang-1) to the endothelial receptor Tie-2 promotes vascular quiescence and the stabilization of endothelial tight junction proteins, such as Occludin

and Zona Occludens-1 (ZO-1), necessary for maintaining the barrier function of the brain microvasculature (11–13). Conversely, angiopoietin-2 (Ang-2), which is rapidly released from small endothelial storage granules called Weibel-Palade bodies, generally acts as a Tie-2 antagonist leading to endothelial activation and vascular leakage (14). Given the opposing roles of these two molecules in vascular function, increased levels of Ang-2 and decreased levels of Ang-1 have been largely associated with cerebral vascular pathogenesis in a multitude of diseases (15, 16). Similarly, a decrease in Ang-1, an increase in Ang-2 and the serum Ang-2:Ang-1 ratio has been well documented in fatal cases of both pediatric and adult CM (17–21). Despite its importance, the mechanisms leading to angiopoietin-Tie axis disruption in CM are poorly understood. Human pro-inflammatory cytokines and pro-coagulation proteins, such as TNF-α and thrombin, have been proposed as responsible for the increase of Ang-2 secretion by endothelial cells (22, 23), but the causative agent responsible for decreased secretion of Ang-1 in CM patients remains unknown.

Smooth muscle cells and pericytes are the main cellular sources for Ang-1 secretion in the brain microvasculature (10). Beyond Ang-1 secretion, pericytes support the microvasculature and promote quiescence through additional roles. Structurally, pericytes wrap around cerebral microvessels and interact with the endothelium through reciprocal ultrastructural membrane protrusions, known as peg-and-socket junctions (24), and secrete extracellular matrix components of the microvascular basal lamina that strengthen microvascular architecture. Functionally, pericytes regulate brain blood flow by controlling vessel diameter through constriction (25). Cerebral pericytes have been implicated in various vascular disorders of the central nervous system. Loss of pericytes from the cerebral vasculature in ischemic stroke and Alzheimer's disease is associated with blood-brain barrier disruption, extravasation of blood components into the brain parenchyma, and neuronal loss (26–28). Similarly, histopathological studies in retinal samples of fatal pediatric CM cases have revealed pericyte damage in regions of *P. falciparum*-iRBC sequestration, suggesting a similar role of these cell types in severe malaria infections (29). Yet, the role of cerebral pericytes in CM pathogenesis and in the dysregulation of the angiopoietin-Tie pathway remains largely unknown.

Bioengineered vascular models are emerging as powerful tools to study disease mechanisms *in vitro.* They have been successfully used to recapitulate many aspects of *in vivo* vascular disease including dysfunction of the angiopoietin-Tie pathway (30), and more recently, malaria pathogenesis, by modeling ligand-receptor interaction of *P. falciparum*-iRBC in microvessels (31) or transcriptional changes on endothelial cells upon exposure to *P. falciparum*-iRBC (32). Here,

97 we have further developed our existent 3D brain microvascular model (31), with the addition of
98 pericytes to create a device that recapitulates *in vivo* interactions between both cell types. We
99 have used this advanced model to understand the molecular basis of angiopoietin-Tie
100 dysregulation in CM. Our results indicate that *P. falciparum*-iRBC and products released during
101 parasite blood stage egress play a role in angiopoietin-Tie dysregulation, and propose brain
102 pericytes as a new player in CM pathogenesis.

103

104 **Results:**

105 ***In vitro* 3D brain microvessel model recapitulates *in vivo* cerebral endothelial-pericyte**
106 **interactions**

107 To investigate the role of cerebral pericytes in *P. falciparum*-mediated vascular pathogenesis, we
108 have generated a 3D brain microvessel model that recapitulates the degree of pericyte coverage
109 of the endothelium present in the brain microvasculature. The device is fabricated in a collagen
110 type I hydrogel containing a microfluidic network with a pre-defined geometry, which is connected
111 to both an inlet and outlet, enabling vessel perfusion (33). Previous incorporation of pericytes in
112 similar bioengineered 3D models involved cellular addition into the collagen hydrogel itself,
113 however, this resulted in sparse interaction of pericytes with the endothelial microvessels (33).
114 Indeed, cerebral pericytes have been shown to cover approximately one third of the brain
115 microvasculature, albeit with slight variations along the brain vascular hierarchical network (34,
116 35). In this model, primary human brain vascular pericytes (HBVP) were seeded directly into the
117 channels along with primary human brain microvascular endothelial cells (HBMEC) at a 5:1
118 endothelial to pericyte ratio (Fig. 1*A*). After 3 days in culture, the two cell types appear to
119 reorganize into two different layers with luminal endothelial cells and mCherry-expressing
120 pericytes wrapping around the endothelial cells (Fig. 1*B*). Pericytes distributed homogenously
121 around the vessel cross-section, with approximately a third of the microvessel surface area
122 covered by pericytes (29.6% of the bottom surface and 27.3% of the top surface) (Fig. 1*C*).
123 Notably, endothelial VE-cadherin junctional labeling is continuous along the vessel luminal
124 surface, suggesting that pericyte presence does not disrupt the endothelial layer (Fig. 1*D*).
125 Furthermore, endothelial cells in the microvessel network express other common cerebral
126 endothelial adherens and tight junction markers, such as β-catenin and ZO-1 respectively (Fig.
127 1*E*). Labeling by α-smooth muscle actin (αSMA) shows that pericytes appear as elongated cells
128 with thin processes stretching over multiple endothelial cells located abluminally between the

endothelial layer and the collagen hydrogel, as suggested by an orthogonal view (Fig. 1*D*). Pericyte cellular identity was confirmed by the expression of a combination of cerebral pericyte cellular markers including αSMA (Fig. 1*D*), platelet derived growth factor receptor β (PDGFRβ) and nerve/glial antigen 2 (NG-2) (Fig. 1*E*) (36, 37). Importantly, labeling of cerebral pericytes colocalized with laminin and collagen IV staining, suggesting that pericytes contribute to the secretion of extracellular matrix components that compose the basal lamina *in vivo* (Fig. 1*E*) (38).

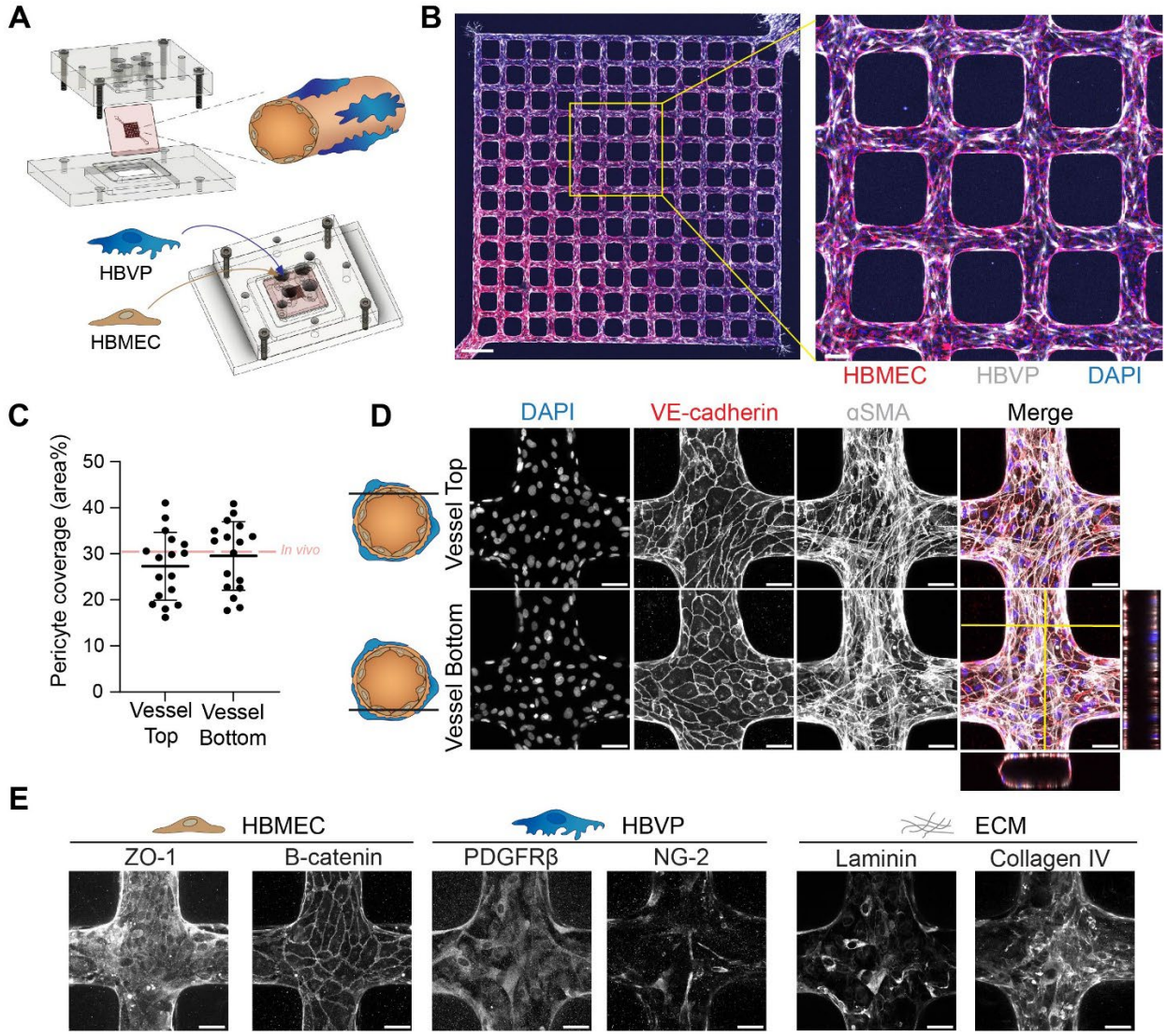

Fig. 1. A microfluidics-based 3D brain microvessel model recapitulates *in vivo* brain vascular architecture and pericyte coverage. *(A)* Schematic depiction of the fabrication pieces and device set-up (top-left), including a representation of resultant endothelial-pericyte interactions (top-right). Schematic depiction of the seeding method used to generate the 3D microvessel model

141 (bottom). *(B)* Immunofluorescence assay (IFA) maximum z-projection of the full network of
142 cellularized channels labeled with Von-Willebrand factor for HBMEC (red), mCherry expressing
143 HBVP (white) and DAPI (blue) (left). Inset highlighting pericyte coverage of the microvessels
144 (right). Scale bars represent 500 μm and 100 μm (Inset) *(C)* Quantification of the percentage of
145 endothelial microvessel area covered by pericytes on either the top or bottom microvessel surface
146 in a z cross-sectional view. Red dashed line represents estimated *in vivo* brain microvascular
147 pericyte coverage. Data points represent quantification of 17 devices with statistical analysis
148 determined by Mann-Whitney U test. Error bars represent mean +/- standard deviation. *(D)* IFA
149 maximum z-projection of VE-cadherin, αSMA, and DAPI labeling on the top and bottom cross-
150 sectional surfaces of microvessels (left). Merge and orthogonal view with VE-cadherin (red),
151 αSMA (white) and DAPI (blue) (right). *(E)* IFA maximum z-projection of brain endothelial markers,
152 ZO-1 and β-catenin, brain pericyte markers, NG-2 and PDGFRβ, and extracellular matrix
153 markers, laminin and collagen IV. Scale bars represent 50 μm in D and E.

154

155 Volumetric electron microscopy has been previously used to characterize *in vivo* 3D ultrastructural
156 interactions between pericytes and endothelial cells of the cerebral microvasculature (24). To
157 characterize the spatial and ultrastructural organization of pericytes and endothelial cells in the
158 model, we utilized Serial Block-Face Scanning Electron Microscopy (SBF-SEM) (39), a volume
159 electron microscopy technique that provides nanometer resolution of samples in a large field of
160 view (40). We imaged a 100 μm segment of a microvessel branch with a 15x15x50 nm xyz
161 resolution, followed by cellular segmentation and rendering. We characterized microvessel
162 coverage of approximately 25 individual pericytes, distinguished from endothelial cells by the
163 presence of a highly granulated cytoplasm (41). Cross-sectional analysis and segmentation of
164 the microvessel revealed an ovoid microvessel morphology, and confirmed the presence of
165 pericytes at the abluminal side of the endothelial cells (Fig. 2*A*). Pericytes acquired a classical
166 bump-on-a-log morphology, with the soma being the thickest region of the cell, and their
167 longitudinal axis aligned with the direction of flow (Fig. 2*B*). Most of the endothelial-pericyte
168 interface is composed of thin pericytic lamellae (100-300 nm thickness) that cover large areas of
169 the endothelial surface, with multiple thin pericytic branches appearing mostly at the cell
170 periphery, as described previously (24). A close up of regions of pericyte-endothelial cell
171 interaction reveal that the membranes of both cell types are in close proximity, even though peg-
172 and-socket junctions were not found (Fig. 2*C*). Although pericytes constitute a heterogenous cell
173 population depending on their location within the vascular branch, their morphology in the model,
174 coverage of endothelial cells, and co-staining of αSMA, PDGFRβ and NG-2 (Fig. 1*D-E*) are
175 reminiscent of ensheathing pericytes commonly found in arterioles (42, 43). Overall, the 3D *in*
176 *vitro* brain microvessel model recapitulates *in vivo* interactions between cerebral endothelial cells

177 and pericytes, both at the tissue and ultrastructural level, that can next be utilized to model the
178 role of pericytes in malaria pathogenesis.

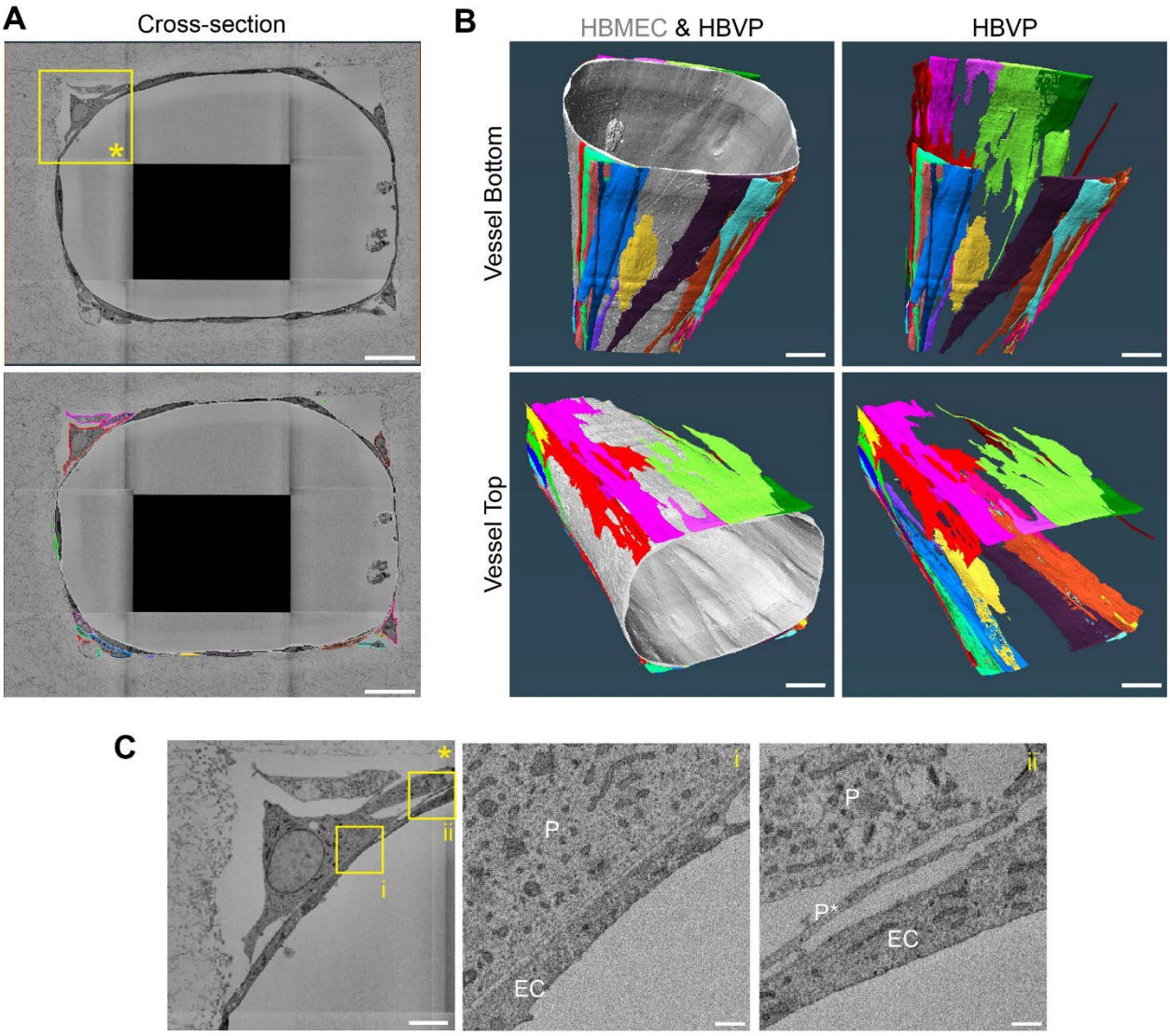

179

180

181 **Fig. 2.** Serial Block-Face Scanning Electron Microscopy reveals ultrastructural interactions
182 between pericytes and endothelial cells. *(A)* A cross-section of the microvessel imaged through
183 the SBF-SEM volume (top) and the corresponding segmentation outlines of the endothelium
184 (grey) and surrounding pericytes (coloured). Scale bars represent 20 µm. *(B)* 3D rendering of the
185 segmented microvessel (grey) and the surrounding pericytes viewed from below and above.
186 Scale bars represent 10 µm. *(C)* Zoomed images of the ROI in A. Insets show ROIs i and ii where
187 pericytes are denoted with "P", endothelial cells by "EC" and pericyte lamellae by "P*". Scale bars
188 represent 5 µm (left) and 500 nm in the insets (center and right).

189

190 ***P. falciparum* egress products increase vessel permeability but only cause minor changes**
191 **in pericyte morphology**

192 Multiple *in vitro* studies have shown that *P. falciparum* products released during malaria parasite
193 egress disrupt the endothelial barrier (44–48). To characterize the impact that these could have
194 on pericyte function, we established a protocol to create media enriched for *P. falciparum*-iRBC
195 egressed products, denoted from here on as iRBC-egress media. Briefly, tightly synchronized
196 schizont stage-iRBCs were purified and allowed to egress in vascular growth media, followed by
197 recovery of the supernatant fraction containing *P. falciparum* soluble products at an estimated
198 concentration of $5x10^7$ruptured iRBC/mL (equivalent to simultaneous egress of approximately a
199 1% parasitemia) (Fig. S1*A*-*B*). We measured the endothelial disruptive properties of iRBC-egress
200 media by the xCELLigence system, which provides real time measurement of cell barrier integrity
201 through impedance. The *P. falciparum* egress products caused a significant, dose-dependent
202 decrease in cell index, a measurement of monolayer barrier function normalized to untreated
203 cells, that reached a maximum disruption at 18 hours (Fig. S1*C*). To elucidate if iRBC-egress
204 media also induces barrier breakdown in the brain 3D microvessel model, we performed
205 permeability assays in a simpler microvessel network which consists of a single 200 µm channel.
206 After perfusion and incubation with iRBC-egress media for 18 hours, *P. falciparum* egress
207 products accumulated on the lateral and bottom walls of the microvessel and appeared as dark
208 spots in brightfield that were DAPI-positive by confocal microscopy, suggesting the presence of
209 hemozoin, food vacuoles and parasite DNA remnants (Fig. 3*A* and *B*). Channels perfused with
210 iRBC-egress media presented a significant increase to 70 kDa FITC-dextran permeability across
211 the entire vessel wall, corresponding to a 6-fold increment compared to vessels perfused with
212 vascular cell media (Fig. 3*B* and *C*).

213 To determine whether increased permeability was associated with physical changes in pericytes,
214 we assessed their cellular morphology in 3D microvessels exposed to iRBC-egress media for 18-
215 hours by SBF-SEM. Pericytes maintained close spatial proximity to the endothelium in the
216 presence of *P. falciparum*-iRBC ghosts, similar to control devices exposed to vascular growth
217 media (Fig. 3*D*). To investigate potential changes in pericyte shape, we isolated and analyzed
218 each 3D rendered pericyte (Fig 3*E*-*F; S2*). Cellular features such as circularity and maximum
219 width did not differ between conditions, however, iRBC-egress media treated pericytes presented
220 fewer branches suggesting a response to iRBC-egress media (Fig. 3*E*-*F*). Altogether, our results

show that *P. falciparum* egress products cause an increase in permeability of the 3D brain microvessel model, accompanied by minor changes in pericyte morphology.

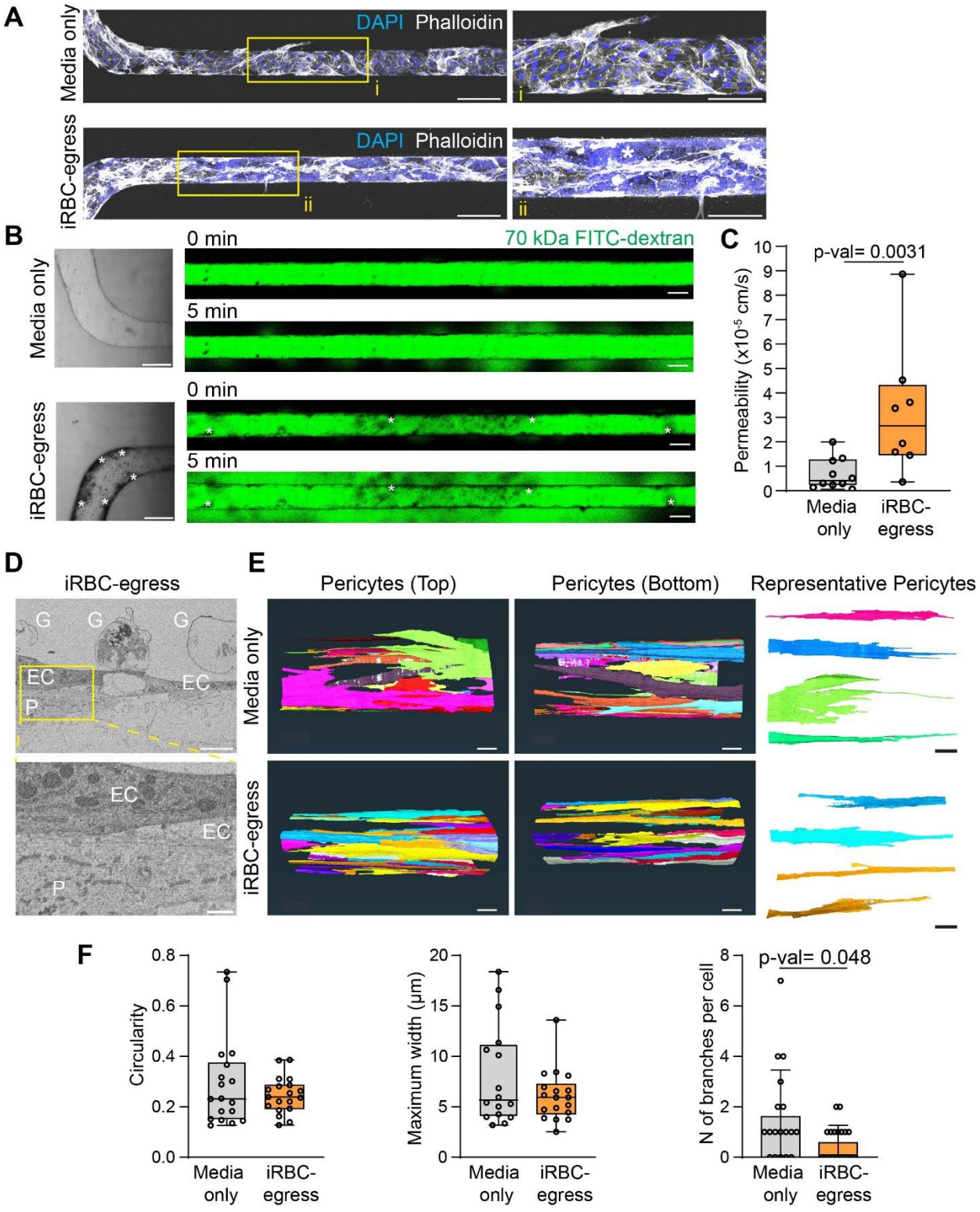

224 **Fig. 3.** iRBC-egress media increases vessel permeability and induces minor morphological
225 changes in pericytes. *(A)* Fluorescence confocal imaging of phalloidin (white) and DAPI (blue) of
226 single channel 3D brain microvessels treated with either media-only or *P. falciparum*-iRBC-egress
227 media for 18-hours. Insets show ROIs of i and ii that highlight endothelial junctions and pericyte
228 coverage (phalloidin). Accumulated DAPI-positive *P. falciparum*-iRBC egress material is denoted
229 by an asterisk. Scale bars represent 200 μm (left) and 50 μm in inset (right). *(B)* Brightfield images
230 near the inlet of 3D brain microvessels after 18-hour incubation with media-only or iRBC-egress
231 media (left). Representative confocal images of 70 kDa FITC-dextran flux into the surrounding
232 collagen 0 and 5 minutes after perfusion (right). Accumulated *P. falciparum*-iRBC egress material
233 is represented with asterisks. Scale bars represents 200 μm. *(C)* Apparent permeability of 70 kDa
234 FITC-dextran in channels treated with media only or *P. falciparum*-iRBC egress media for 18-
235 hours. Data points represent 8 individual devices. *(D)* SBF-SEM image and zoomed ROI of
236 microvessels treated with iRBC-egress media. Pericytes are denoted as "P", endothelial cells by
237 "EC" and iRBC ghosts by "G". Scale bar represents 2 μm (top) and 500 nm in inset (bottom). *(E)*
238 3D rendering of pericytes segmented from microvessels treated with media-only or iRBC-egress
239 media and imaged with SBF-SEM (left). Representative segmented pericytes for morphology
240 analysis (right). Scale bar represents 10 μm. *(F)* Circularity, maximum width and number (N) of
241 branches analysis of 16-18 segmented pericytes. Box and whisker plots display the median, 25th
242 and 75th percentiles and the minimum and maximum data points, and statistical significance was
243 measured by Mann-Whitney U test in both C and F.

244 ***P. falciparum*-iRBCs induce dysregulation of the angiopoietin-Tie axis**

245 To determine whether parasite egress products are a major driver of angiopoietin-Tie axis
246 disruption characteristic of CM (17–20, 49), we used a Luminex assay to measure secreted
247 protein concentrations in microvessel supernatants recovered after 18-hour incubation with iRBC-
248 egress media. Remarkably, we observed a substantial decline of Ang-1 secretion by pericytes,
249 with concentrations nearly reaching the baseline level detected in acellular vascular growth media
250 (Fig. 4*A*). Consistent with recent studies on 2D HBMEC monolayers (22), iRBC-egress media
251 incubation did not result in increased Ang-2 secretion. Indeed, we quantified a significant
252 decrease in Ang-2 secretion (Fig. 4*A*). Despite Ang-2 decrease, a significant increase in the Ang-
253 2/Ang-1 ratio was found, after Ang-1 and Ang-2 concentrations were subtracted against
254 concentrations found in the acellular vascular growth media (Fig. 4*A*). Additionally, we observed
255 a decrease in 3D microvessel secretion or shedding of other vascular factors important for
256 endothelial-pericyte interaction, such as Neural cadherin (N-cadherin) and Tissue Inhibitor of
257 Metalloproteinase-1 (TIMP-1) (Fig. S3*A*). Conversely, we detected no changes in Vascular
258 Endothelial Growth Factor (VEGF), Tie-2, Angiopoietin-like-4 (ANGPTL4), Platelet Derived
259 Growth Factor-BB (PDGF-BB), Interleukin-8 (IL-8) or Chemokine Ligand-1 (CXCL-1) after 18-
260 hour incubation with iRBC-egress media (Fig S3).

261 To validate whether changes in the angiopoietin-Tie axis occur physiologically following *P.*
262 *falciparum* blood stage egress within the microvasculature, we perfused the 3D brain
263 microvessels with schizont stage *P. falciparum*-iRBC for 30 minutes followed by a 10-minute
264 wash. After an 18-hour incubation period, supernatants were again recovered and analyzed by
265 Luminex. Similar results were obtained, with a reduction in both Ang-1 and Ang-2 secretion and
266 an increase in the Ang-2/Ang-1 ratio (Fig. 4*B*). Altogether, these results suggest that *P.*
267 *falciparum*-iRBC hamper Ang-1 secretion by pericytes, revealing a previously unappreciated role
268 of pericytes in the dysregulation of the angiopoietin-Tie axis in cerebral malaria.

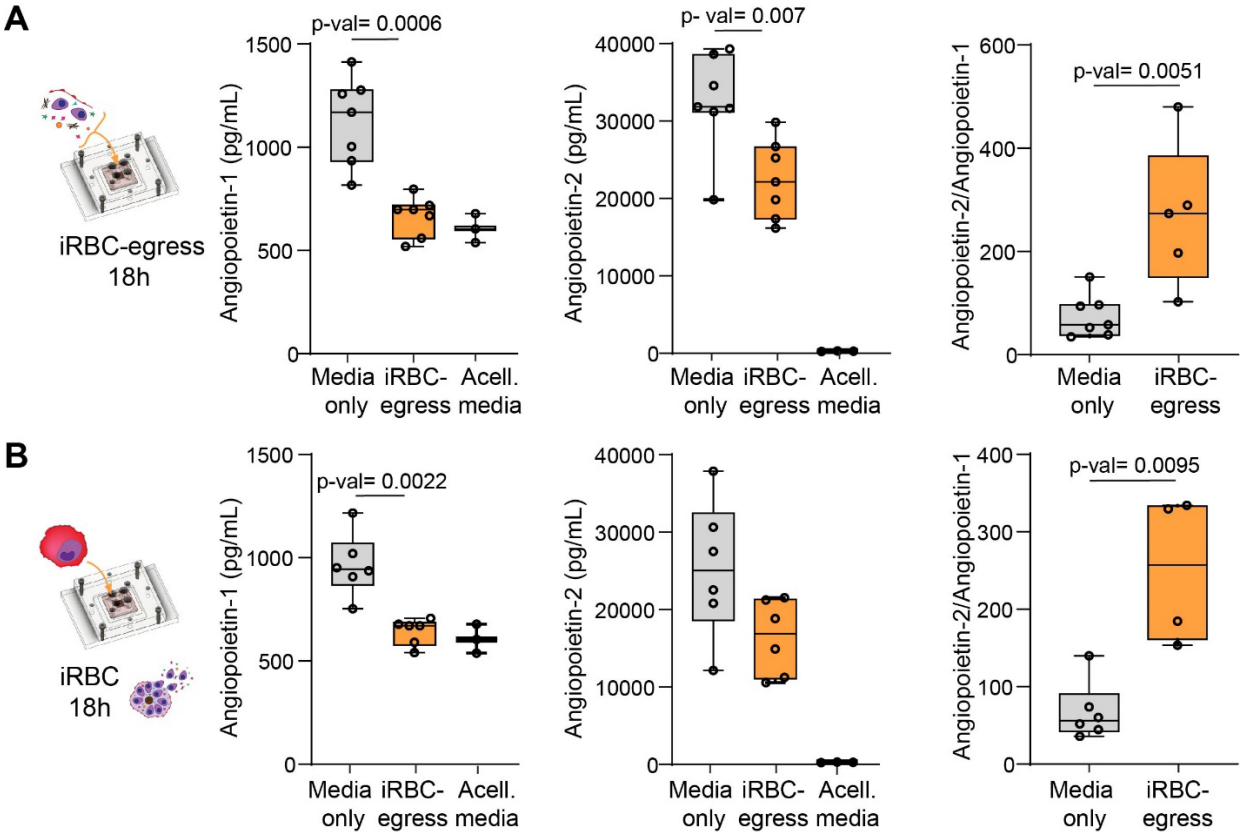

269

270 **Fig. 4.** *P. falciparum*-iRBC-egress media and intact *P. falciparum*-iRBC induce angiopoietin-Tie
271 axis dysregulation. *(A)* Ang-1 and Ang-2 concentrations measured from 3D brain microvessels
272 treated with media-only, iRBC-egress media for 18-hours or from acellular media before culture
273 (Acell. Media) (left and center). Ang-2: Ang-1 ratio in supernatants collected from 3D brain
274 microvessels normalized to corresponding acellular media protein concentrations (right). *(B)* Ang-
275 1 and Ang-2 concentrations measured from 3D brain microvessels treated with media-only, *P.*
276 *falciparum*-iRBC for 18-hours or from acellular media before culture (Acell. Media) (left and
277 center). Ang-2: Ang-1 ratio in supernatants collected from 3D brain microvessels normalized to
278 corresponding acellular media protein concentrations (right). Box and whisker plots display the
279 median, 25th and 75th percentiles and the minimum and maximum data points in A and B. Data
280 points represent supernatants pooled from 2-3 devices in 6-7 independent experiments and were

281 analyzed by Mann-Whitney U test. Acellular media measures were obtained from 3 independent
282 aliquots. Data points in which Ang-1 concentrations measured from 3D brain microvessels were
283 below the concentrations in acellular media were removed to calculate the Ang-2: Ang-1 ratio.

284 **Recombinant Ang-1 partially protects against endothelial barrier breakdown by iRBC-**
285 **egress media**

286 Given the key role of Ang-1 to promote vascular quiescence and endothelial barrier formation we
287 investigated whether Ang-1 supplementation could protect against the barrier disruptive effects
288 of iRBC-egress media. First, we measured barrier disruption by xCELLigence in a 2D *in vitro*
289 endothelial culture in the absence of pericytes. Furthermore, the 18-hour pre-treatment of rAng-1
290 to resting endothelium caused a non-significant minor decrease in endothelial permeability.
291 Conversely, an 18-hour pre-treatment of recombinant Ang-1 (rAng-1), prior to the incubation with
292 iRBC-egress media and rAng-1, partially protected against endothelial barrier disruption (Fig. 5*A*-
293 *C*). While both iRBC-egress media conditions follow parallel endothelial breakdown trajectories,
294 rAng-1 addition dampened the maximum levels of disruption by iRBC-egress media, and was
295 followed by a faster recovery to endothelial monolayer baseline levels (Fig. 5*B*). Indeed, pre-
296 treatment with rAng-1 conferred a 35% barrier breakdown protection after normalization to the
297 untreated endothelial condition (Fig. 5*C*). Nevertheless, shorter pre-treatment periods with rAng-
298 1 (1-hour) did not protect against iRBC-egress media disruption, suggesting that the
299 establishment of endothelial protective pathways is not immediate (Fig. S4).

300 Next, we tested the protective capacity of rAng-1 against iRBC-egress products in the 3D
301 microvessel model (Fig. 5*D*). While 3D microvessel permeability values to 70 kDa FITC-dextran
302 presented a 6.5-fold increase upon exposure to iRBC-egress media, permeability values only
303 increased by 1.5-fold following an iRBC-egress media challenge after an 18-hour pre-treatment
304 with rAng1 (Fig. 5*E*-*G*). Overall, rAng-1 conferred statistically significant protection to the barrier
305 breakdown properties exerted by iRBC-egress media (Fig. 5*G*). Taken together, pre-treatment
306 with rAng-1 partially protects against microvascular permeability caused by *P. falciparum* egress
307 products, both in 2D and 3D, highlighting the importance that a decrease in Ang-1 could have in
308 CM pathogenesis.

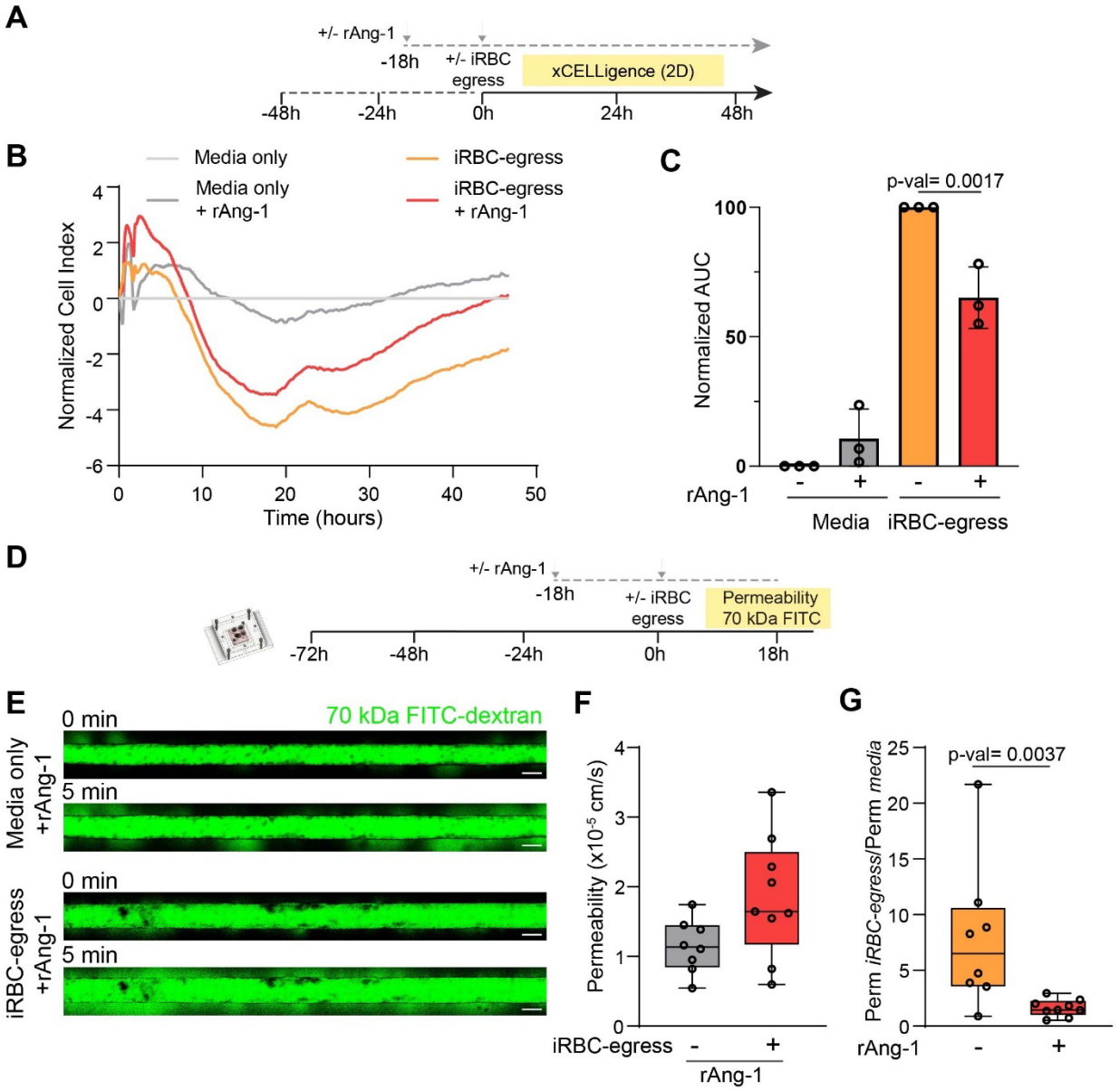

Fig. 5. Recombinant Ang-1 (rAng-1) partially protects against increased permeability induced by iRBC-egress media. *(A)* Experimental outline of the rAng-1 pre-treatment permeability experiment measured in 2D HBMEC monolayers in the absence of HBVP. *(B)* Representative recording data of xCELLigence measurements taken after an 18-hour +/- rAng-1 pre-treatment followed by +/- iRBC-egress media addition. All conditions were normalized to the media only control. *(C)* Area under the curve analysis of 3 independent experiments run in triplicate with iRBC-egress media normalized as 100. Error bars are mean +/- standard deviation. Statistical significance is measured by repeated measures one-way ANOVA test with Dunnett's multiple comparisons test. *(D)* Experimental outline of the rAng-1 pre-treatment permeability experiment on 3D brain microvessels. *(E)* Confocal image of the 70 kDa FITC-dextran flux into the surrounding collagen at 0 and 5 minutes after dextran perfusion. Images correspond to a representative rAng-1 pretreated microvessel exposed to either media-only or iRBC egress media for 18 hours. Scale bars represent 200 μm. *(F)* Apparent permeability of 70 kDa FITC-dextran in channels pretreated

323 with rAng-1 followed by 18-hour media-only or iRBC egress media treatment in 8-9 individual
324 devices per condition. *(G)* Change in permeability following rAng-1+/-iRBC-egress media
325 treatment normalized by the median value of either the rAng-1+/-media only condition. Box and
326 whisker plots display the median, 25th and 75th percentiles and the minimum and maximum data
327 points in F and G. Statistical significance was analyzed by Mann-Whitney U test.

328 **Discussion:**

329 Disruption of the angiopoietin-Tie axis is a common feature in cerebral malaria patients, often
330 associated with disease severity and fatality (18, 20). This dysregulation is also found in pediatric
331 and adult severe malaria patients without cerebral complications (17, 19) or in placental malaria
332 (50). Central to this pathway are cerebral pericytes, an Ang-1 secreting cell type that is located at
333 the interface between the vasculature and brain parenchyma, yet largely understudied in the
334 context of cerebral malaria. Here, we developed a 3D brain microvessel microfluidic model that
335 recapitulates the high pericyte coverage present in the brain microvasculature. Exposure of the
336 3D brain microvessels to *P. falciparum*-egress products caused an increase in vascular
337 permeability accompanied by a decrease in Ang-1. Furthermore, we showed that pre-treatment
338 with rAng-1 could, at least, partially protect against endothelial barrier breakdown. Taken together,
339 these results suggest that the cessation of Ang-1 release upon exposure to iRBC-egress products
340 further contributes to microvessel disruption.

341 The bioengineered 3D model provides important vascular mechanical cues, including estimated
342 flow and extracellular matrix stiffnesses present in the human brain. We could reproduce the high
343 pericyte coverage found in brain capillaries by co-seeding primary cerebral endothelial cells and
344 pericytes through the microfluidic network. Simultaneous cell seeding, at a ratio of 5:1 (endothelial
345 cells: pericytes), did not prevent the formation of an intact luminal endothelial monolayer that
346 presents continuous labeling of adherens and tight junctional markers. SBF-SEM microscopy
347 showed that both cell types sit at nanoscale distance, with the presence of thin lamellae extending
348 from the pericyte soma covering large areas of the endothelium. Yet, despite close proximity, the
349 recently well-described reciprocal peg-and-socket junctions were absent in the model (24).
350 Overall, the 3D brain microvessel model recapitulates pericyte-endothelial interactions found in
351 human brain vasculature making it suitable to study the role of pericytes in CM pathogenesis.

352 *P. falciparum* products released during blood stage egress have been shown to possess barrier
353 breakdown capabilities on 2D endothelial monolayers grown on plastic. Proposed barrier
354 disruptive *P. falciparum*-iRBC egress products include merozoite proteins, histones, heme,
355 hemozoin and *P. falciparum* histidine rich protein 2 (22, 44–48, 51). However, their effects on
356 pericytes remain unexplored. In this study, we confirmed that these products are disruptive in a

357 microfluidics-based 3D brain microvessel model in the presence of pericytes. Pericytes play an
358 important role in maintaining vascular homeostasis. For example, loss of pericytes from the
359 cerebral vasculature leads to increased permeability in mouse models (52). Furthermore,
360 dysregulation of cerebral pericytes and detachment from the vasculature have been observed in
361 other cerebral vasculature pathologies including stroke and Alzheimer's disease (26, 27). In our
362 study, we did not observe gross differences on pericyte morphology or loss of vascular coverage
363 upon treatment with iRBC-egress media. Nevertheless, pericytes from iRBC-egress media -
364 treated 3D microvessels did display subtle morphological changes, having significantly less
365 branches. The relevance of these minor ultrastructural modifications in vascular barrier
366 dysfunction could imply molecular mechanisms of disease. For example, Luminex quantification
367 upon stimulation with iRBC-egress media in the 3D brain microvessel model revealed a significant
368 reduction in N-cadherin shedding. This could point towards reduced functional endothelial-
369 pericyte interaction upon short-term incubation with *P. falciparum*-egress products. Future studies
370 should explore whether exposure to *P. falciparum* for longer timepoints recapitulates phenotypes
371 observed in post-mortem samples of cerebral malaria patients such as vacuolization (53) or
372 pericyte loss (29). Nevertheless, our results point towards a loss of integrity at the endothelial and
373 pericyte interface.

374 Ang-1 and Ang-2 have been considered in the past as potential biomarkers of cerebral malaria
375 (54). Ang-1 has excellent predictive power to distinguish malaria severity scores (19) or malaria
376 from other CNS febrile diseases (55). Nevertheless, the underlying mechanism of Ang-1 decrease
377 in CM remains unknown, as previous *in vitro* studies overlooked the effect that iRBCs could exert
378 on brain pericytes. To our knowledge, our study is the first one to report that *P. falciparum*
379 products released upon iRBC egress halt Ang-1 secretion by pericytes. A complementary
380 hypothesis for Ang-1 decrease in CM could be that severe thrombocytopenia, commonly
381 associated with cerebral complications in *P. falciparum* infections (7), could play an additional role
382 as platelets are another major source of serum Ang-1 (56). In light of this, it is likely that both the
383 effect of *P. falciparum*-iRBC on perivascular cells and thrombocytopenia could work in concert to
384 further contribute to a widespread decrease of Ang-1 levels. As for the mechanism of Ang-1
385 secretion cessation, the presence of accumulated light scattering, DAPI-positive iRBC-egress
386 material suggest a role of parasitic DNA or hemozoin, yet further studies are necessary to identify
387 which iRBC-egress derived component is responsible for altered signaling pathways in pericytes.
388 Nevertheless, our results highlight brain pericytes as a new player in the development of CM
389 through dysregulation in the secretion of Ang-1.

390 The use of recombinant Ang-1 as an adjunctive therapeutic against CM has long been of interest
391 (49) because of its role in strengthening endothelial tight junctions, as well as, upregulating anti-
392 apoptotic and anti-inflammatory pathways (57). Interestingly, we showed that pre-incubation of
393 human microvessels with recombinant Ang-1 partially protected against iRBC-egress mediated
394 barrier breakdown. Nevertheless, the failure to achieve complete protection upon rAng1
395 supplementation hints at the existence of other pathogenic mechanisms involved in cerebral
396 malaria-induced barrier breakdown. While the concentration of recombinant Ang-1 utilized in this
397 study was supraphysiological compared to peripheral blood samples, it is quite likely that
398 peripheral blood concentrations underestimate local concentrations at the endothelial-pericyte
399 interface. In our model, protection was only achieved after a pre-incubation of 18-hours,
400 suggesting that downstream signaling through the Tie2 receptor, such as PI3K/Akt signaling, is
401 required (10). Future interventions targeting the angiopoietin-Tie axis should focus on approaches
402 that reverse microvascular dysfunction after exposure to *P. falciparum.* As a proof of concept,
403 recombinant Ang-1 has previously been used as a treatment in a rodent experimental cerebral
404 malaria model after onset of disease, preserving blood-brain barrier integrity, and leading to a
405 significantly increased survival rate (49). Although we did not observe protection after short term
406 exposure, our findings point towards a mechanistic role of Ang-1 in protecting against iRBC
407 egress-mediated endothelial barrier breakdown, further highlighting Ang-1 alteration as a
408 functional contributor to CM pathogenesis.

409 Clinical studies have shown a lack of correlation between Ang-2 levels and iRBC microvascular
410 obstruction in the rectal microvasculature (58) or iRBC sequestration in brain post-mortem
411 samples (59). Similarly, our study confirms that iRBC sequestration in 3D brain microvessel
412 models does not directly cause Ang-2 secretion by endothelial cells. Furthermore, this result is in
413 concordance with a recent study that showed that Ang-2 is not secreted in response to *P.*
414 *falciparum* lysate products, but rather occurs following endothelial activation with TNF (22). Other
415 studies have shown Ang-2 release as a result of thrombin incubation or hypoxia (23, 60),
416 conditions that have also been associated with CM pathogenesis. Altogether, our study is in
417 agreement with previous reports suggesting that *P. falciparum* sequestration does not play a
418 direct role in the secretion of Ang-2, which instead is more likely a consequence of the activation
419 of host pro-inflammatory factors.

420 To note, our study has several limitations, including the low-throughput of the model or the
421 impossibility to grow the devices for long periods of time, hence preventing the modelling of long-
422 term disruptive mechanisms, such as pericyte loss. An additional limitation of our model is the

423 absence of other cells that could play an important role in maintaining the angiopoietin-Tie axis.
424 For example, Ang-1 secretion has been described in other brain and blood cell types, such as
425 smooth muscle cells (61, 62), platelets and more recently, neurons and astrocytes (63). Yet, one
426 of the major advantages of *in vitro* bioengineered models is the opportunity to sequentially
427 introduce different components that, independently or collectively, could play a role in a complex
428 and multifaceted disease such as CM. In light of this, future iterations of the model could introduce
429 other cell types that produce Ang-1 or incorporate pro-inflammatory cytokines or thrombin, to
430 concurrently model the functional consequence of increased secretion of Ang-2 by endothelial
431 cells.

432 In summary, our study highlights the role that pericytes could have in the development of CM
433 pathogenesis by showing for the first time that egress of *P. falciparum*-iRBC interrupt Ang-1
434 secretion by pericytes. In addition, our findings confirm that external addition of Ang-1 partially
435 protects against the increase in vascular permeability mediated by *P. falciparum* egress products,
436 suggesting that interventions involving the angiopoietin-Tie axis could be part of a multi-targeted
437 adjunctive therapy against CM.

438

439 **Materials and Methods:**

440 **Parasite lines**:

441 HB3var03 variant *P. falciparum* parasites (dual ICAM-1 and EPCR binding), regularly panned and
442 monitored for appropriate PfEMP1 expression, were cultured in human B+ erythrocytes in RPMI
443 1640 medium (GIBCO) supplemented with 10% human type AB-positive plasma, 5mM glucose,
444 0.4 mM hypoxantine, 26.8 mM sodium bicarbonate and 1.5 g/L gentamicin. Parasites were grown
445 in sealed top T75 flasks in a gas mixture of 90% N_2, 5% CO_2 and 1% O_2. To maintain synchronous
446 cultures, parasites were synchronized twice a week in their ring stage with 5% sorbitol and once
447 a week in their trophozoite stage with 40 mg/mL gelaspan (Braun).

448 ***P. falciparum*-iRBC egress media preparation**:

449 Late-stage *P. falciparum*-iRBC (schizonts, parasitemia of 5-10%), synchronized in a 6-hour
450 window, were purified by use of 40 mg/mL gelaspan gradient separation to a final purity of >60%
451 parasitemia. The enriched *P. falciparum*-iRBC were then placed in complete RPMI media
452 containing 1 μM compound 2, a reversible PKG inhibitor that inhibits iRBC egress (kindly donated
453 by Michael Blackman, The Francis Crick Institute), at a concentration of 50 million *P. falciparum*-

454 iRBC/mL. After 5 hours, compound 2 containing media was removed and the parasites were
455 resuspended at a concentration of 100 million *P. falciparum*-iRBC/mL in vascular growth media,
456 put into a sealed top T25 flask, gassed and left in the incubator overnight on a shaker set to 50
457 rpm to facilitate parasite egress. The resulting parasite egress efficiency was assessed by a
458 hemocytometer count and blood smear, and was then concentrated to a working concentration
459 of 50 million ruptured *P. falciparum*-iRBC/mL. The resulting iRBC-egress media is spun at 1000
460 rpm to remove cellular debris and flash frozen in liquid nitrogen until used. This concentration was
461 chosen as this value is equivalent to a circulating parasitemia of 1%, concentrations frequently
462 found in malaria patients.

463 **Primary human brain microvascular endothelial cell and primary human brain vascular**
464 **pericyte culture**:

465 Primary HBMEC (Cell Systems; ACBRI 376) were cultured according to the manufacturer's
466 recommendations in complete endothelial growth media-2MV (Lonza) containing 5% fetal bovine
467 serum. Cells were split using Trypsin/EDTA. When 90% confluent, HBMEC were seeded on 15
468 µg/mL Poly-L-lysine (P8920, Sigma) coated T75 flasks. Primary HBVP (ScienCell) were cultured
469 according to the manufacturer's recommendations in basal pericyte media supplemented with 1%
470 pericyte growth supplement, 1% penicillin/streptomycin and 2% fetal bovine serum (ScienCell).
471 Cells were split using Trypsin/EDTA when 90% confluent, seeded on 15 µg/mL Poly-L-lysine
472 coated T75 flasks, and maintained in a humidified incubator at 37 °C and 5% CO_2. All experiments
473 were conducted with HBMEC and HBVP with a passage number of 7-9.

474 **mCherry lentivirus transduction**:

475 HBVPs were grown in a T75 flask to a ~90% confluency and incubated with lentiviral particles
476 containing a mCherry vector (kindly donated by Kristina Haase Lab, EMBL Barcelona) in serum
477 free pericyte media at a multiplicity of infection of 10. After 24 hours, the lentivirus particles were
478 removed by washing once every 24-hours for a 2-day period. mCherry-positive cells were then
479 selected by fluorescence-activated cell sorting, expanded and froze down for future experiments.

480 **3D brain microvasculature model fabrication**:

481 Type 1 collagen was extracted from rat tails, dissolved in 0.1% acetic acid, lyophilized in a freezer
482 dryer (Labconco Freezone 2.5 Plus) and resuspended at 15 mg/mL in 0.1% acetic acid for
483 storage. The stock collagen solution-0.1% acetic acid solution was neutralized and diluted to 7.5
484 mg/mL on ice. A 13 by 13 channel grid or single channel pattern were negatively imprinted into

485 the collagen hydrogel by soft lithography using a PDMS stamp, and inlet and outlets were created
486 by insertion of stainless-steel dowel pins. The top pre-patterned collagen hydrogel contained in a
487 plexiglass top jig is sealed to a flat collagen-layered bottom that sits on a coverslip and a plexiglass
488 bottom jig. The assembly creates perfusable 120 μm diameter microvessels (grid design) or 200
489 μm diameter microvessels (single channel design), as described previously (33, 64). Prior to cell
490 seeding, the channels were incubated with vascular growth media, consisting in EGM-2MV
491 (Lonza) supplemented with 1x pericyte and 1x astrocyte growth factors (ScienCell) for 1 hour.
492 Primary HBMECs and HBVPs, or mCherry-positive HBVPs (for pericyte coverage analysis), were
493 resuspended at concentrations of 7 million cells/mL and mixed to a ratio of 5:1 HBMECs to
494 HBVPs. The cell mixture was then seeded into the inlet in 8 μL increments and driven through the
495 microfluidic network by gravity-driven flow. Cells were perfused twice from either the inlet or outlet
496 until the channels were completely covered with adhered cells. Media was then removed and
497 devices were flipped upside down for 1-hour to ensure even cell distribution on the top and bottom
498 of the channels. Microvessels were cultured for 3 days before being used in experiments with
499 media change every twice per day by gravity driven flow.

500 **Immunofluorescence microscopy**:

501 Microvessel labeling was performed by gravity driven flow. Microvessels were fixed with 3.7%
502 paraformaldehyde (PFA) in PBS for 15 minutes followed by three 10-minute washes with PBS.
503 Next microvessels were incubated with Background Buster (Innovex) for 30 minutes and then
504 permeabilized with blocking buffer (0.1% Triton X-100 and 2% bovine serum albumin in
505 phosphate-buffered saline (PBS)). Primary antibodies including rabbit anti-αSMA-555 (EPR5368,
506 Abcam), mouse anti-vWF (sc-365712, Santa Cruz), mouse anti-ZO-1 (Invitrogen, 10017242),
507 rabbit anti-β-catenin (Cell Signaling, 9587S), mouse anti-PDGFRβ (Abcam, ab69506), mouse
508 anti-NG-2 (Invitrogen, 10424493), rabbit anti-laminin (Abcam, ab11575), rabbit anti-collagen IV
509 (Abcam, ab6586)), mouse anti-VE-cadherin (sc-52751, Santa Cruz), and Phalloidin-647
510 (Invitrogen, A22287) were diluted in blocking buffer at 1:100 and incubated overnight at 4 °C.
511 After three 10-minute PBS washes, secondary antibodies including goat anti-mouse Alexa Fluor
512 488 (A11001, Invitrogen), goat anti-rabbit Alexa Fluor 488 (Invitrogen, A-11008), goat anti-mouse
513 Alexa Fluor 594 (Invitrogen, A-11005), goat anti-rabbit Alexa Fluor 594 (Invitrogen, A-11012),
514 goat anti-mouse Alexa Fluor 647 (A21235, Invitrogen), goat anti-rabbit Alexa Fluor 647
515 (Invitrogen, A-21244) and 2 mg/mL DAPI (D21490, Invitrogen) were diluted at 1:250 in 2% bovine
516 serum albumin and 5% goat serum containing PBS, and incubated at room temperature for 1
517 hour. Microvessels were washed 6 times with PBS for 10 minutes each and then imaged on a

518 Zeiss LSM 980 Airyscan 2. Image stacks were acquired with 3 µm or 10 µm z-step size for single
519 or tile scan images respectively. Z-projections and further threshold analysis was done using Fiji
520 (ImageJ v1.54f) software.

521 **Pericyte coverage analysis:**

522 Tile scan images of the microvessel network with mCherry-positive HBVP and vWF-labeled
523 HBMEC were acquired as described above. Images were divided into two stacks, one being the
524 top half of the microvessels of the network and the other the bottom half. Next, Z-projections of
525 the top and bottom surfaces of the network were generated. The percentage of endothelial
526 surface that was covered by pericytes was calculated by creating a mask of both the mCherry
527 HBVP and the vWF-positive HBMEC.

528 **Serial Block-Face Scanning Electron Microscopy:**

529 Microvessel devices were grown for 3 days, then treated with iRBC-egress media or vascular
530 growth media for 18hours, and then fixed by adding 2% PFA and 2.5% glutaraldehyde (GA) to
531 the device inlet for 30-minutes and washed twice with EGM-2MV at 37 °C. The collagen hydrogel
532 was then carefully removed from the plexiglass jig and microvessel regions exposed to low shear
533 stress were cut out and fixed with a secondary fixative solution (2% PFA, 2.5% GA, 0.25 mM
534 $CaCl_2$, 0.5 mM MgCl, 5% sucrose in a pH 7.4 0.1 M Cacodylate buffer) overnight at 4 °C, and
535 then rinsed twice for 15-minutes with 0.1 M Cacodylate buffer. Samples were post-fixed in a
536 reduced Osmium solution (1% OsO_4, 1.5% K_3FeCN_6 in 0.065 M Cacodylate buffer) for 2-hours at
537 4 °C followed by six 10-minute washes in dH_2O. Post-staining consisted of subsequent incubation
538 steps of 1% thiocarbohydrazide in dH_2O, 2% Osmium tetroxide in dH_2O, and 1% Uranyl acetate
539 in dH_2O, aided by a PELCO Biowave Pro+ (Ted Pella) containing a SteadyTemp Pro and
540 ColdSpot set to 20 °C at 7x 2 minute cycling on-off at 100 W under vacuum, with dH_2O rinses in
541 between steps once in a fume hood and twice in the microwave at 250 W for 40 s without vacuum.
542 The stained samples were then dehydrated by serial additions of 30, 50, 80, and 100% ethanol
543 solutions in the microwave at 250 W for 40 s without vacuum with ColdSpot set to 4 °C, infiltrated
544 with EPON 812 hard epoxy resin in steps of 25, 50, 75, 90, and 3x 100% resin diluted in ethanol
545 with each step in the microwave at 150 W for 3 minutes under vacuum and polymerized at 60 °C
546 for 48 hours. The sample was trimmed (UC7, Leica Microsystems) using a 90° cryo-trimmer
547 (Diatome) to generate a small block face. The resulting resin block was mounted on a pin stub
548 using silver conductive epoxy resin (Ted Pella). The SBF-SEM acquisition was performed with a
549 Zeiss Gemini2 equipped with a Gatan 3view microtome and a focal charge compensation device

550 (Zeiss). The SEM was operated at 1.5 kV 300 pA, using a pixel size of 15 nm, a slice thickness
551 of 50 nm and a dwell time of 1.6 µs. The SBF-SEM acquisition was performed using the software
552 SBEMimage (65). The acellular center of the lumen was not imaged to save imaging time.
553 Following acquisition, sections and tiles obtained were aligned and blended using a published
554 method for assembly, stitching and alignment of large EM datasets (66). Aligned images were
555 then binned to 22 by 22 by 250 nm^3 in xyz and segmentation was then performed using the
556 software package Amira (Thermo Fischer Scientific). Primary HBVP and HBMEC were
557 segmented semi manually using the magic wand and brush tool to segment every fifth section
558 followed by use of the interpolation tool to segment the entire volume. The resulting segmented
559 microvessels were rendered using the generate surfaces module for 3D visualization.

560 ***P. falciparum*-iRBC and iRBC-egress media perfusion:**

561 All experiments were done in 3D microvessel devices grown for 3 days. Schizont-stage *P.*
562 *falciparum*-iRBC were purified to >60% parasitemia by 40 mg/mL gelaspan and the resulting
563 enriched population was diluted in vascular growth media to 50 million iRBC/mL (same
564 concentration as the *P. falciparum*-iRBC-egress media). 200 µL of *P. falciparum*-iRBC or *P.*
565 *falciparum*-iRBC-egress media was added into the device inlet and perfused by gravity flow for
566 30-minutes with the outlet effluent being reintroduced to the inlet every 10 minutes. Microvessels
567 treated with intact *P. falciparum*-iRBC (but not *P. falciparum*-iRBC-egress media), were then
568 washed for 10 minutes with vascular growth media. Both conditions were incubated overnight for
569 18 hours. Supernatant was then removed from the outlet and pooled for Luminex analysis, and
570 3D brain microvessels were used for permeability studies or fixed for imaging with 3.7% PFA for
571 15 minutes (see section immunofluorescence microscopy).

572 **Fluorescent dextran-based permeability assay:**

573 Single channel microvessel devices were grown for 3 days, then perfused and incubated for 18
574 hours with either vascular growth media or *P. falciparum*-iRBC-egress media as described above.
575 To determine resulting changes in permeability, they were perfused with a 70 kDa FITC-dextran
576 solution as follows: the device was washed 1x with PBS and placed in a Zeiss LSM 980 Airyscan2
577 confocal microscope with a temperature and CO_2 controlled imaging chamber (37 °C, 5% CO_2).
578 PBS was aspirated and 100 µL of 70 kDa FITC-dextran solution (100 µg/mL) in PBS was pulled
579 from the inlet to the outlet at 6.5 µL/min flow rate using a syringe pump (Harvard Apparatus PHD
580 2000). Tilescan confocal images of the entire channel were taken every 30 seconds for 5 minutes
581 once the channel had been filled with FITC dextran. In devices pre-treated with recombinant Ang-

582 1 (923-AB-025, R&D Systems), pre-incubation occurred at 18-hours, starting on day 2. To
583 compare changes in permeability following *P. falciparum*-iRBC-egress media treatment in the
584 presence or absence of rAng-1, the ratio between untreated and treated devices with *P.*
585 *falciparum*-iRBC was calculated using median values for normalization.

586 **Quantification of apparent permeability:**

587 Apparent permeability is determined as the flux of fluorescently labeled dextran across the
588 microvessel wall into the surrounding collagen hydrogel. All steps of permeability analysis were
589 performed using ImageJ. By using the following equation:

590 $$Papp = \frac{1}{I_{Vt1} - I_{Tt1}} \times \frac{I_{Tt2} - I_{Tt1}}{\Delta t} \times \frac{A_{\text{lateral tissue}}}{P}$$

591 The apparent permeability (P_{app}) was calculated using the fluorescence intensity inside the vessel
592 (I_V) and in the surrounding collagen hydrogel (I_T) at two time points t1 (0 minutes after the vessel
593 is filled with dextran) and t2 (5 minutes after the vessel is filled). Δt is the change in time, $A_{lateral}$
594 $_{tissue}$ is the area of the collagen hydrogel being examined and P is the perimeter of the microvessel.
595 To account for *P. falciparum*-iRBC-egress material that appears dark even in the presence of 70
596 kDa FITC-dextran, regions of *P. falciparum*-iRBC-egress material were excluded from the
597 calculation of the fluorescence intensity inside the vessel (I_V) by using ImageJ median smoothing
598 and the magic wand tool to select only the area of the channel without *P. falciparum*-iRBC-egress
599 material.

600 **Serial Block-Face Scanning Electron Microscopy pericyte morphology analysis:**

601 3D-rendered pericyte meshes, segmented from SBF-SEM images of microvessels treated with
602 either media alone or iRBC-egress media, were generated using Amira. Following segmentation,
603 the meshes were exported as *STL* files and processed with a custom-developed Python script,
604 designed to quantify aspects of pericyte morphology, including mesh circularity and maximum
605 width (67). Firstly, the 3D pericyte meshes were mapped onto a 2D plane through principal
606 component analysis (PCA), effectively reducing the data's dimensionality while retaining its most
607 significant morphological features. This mapping uses the two principal components that
608 encapsulate the dimensions with the maximum variance in the 3D mesh, thus ensuring the
609 conservation of structural information. Subsequently, convex hull analysis (68) was applied to
610 delineate the pericyte mesh boundaries, providing a clear representation of each structure's
611 shape by which circularity and maximum width could be measured. The circularity of each mesh
612 is calculated using the convex hull, by assessing the ratio of the area enclosed by the hull to the

613 square of the hull perimeter, with the formula for circularity given as $4\pi \times Area/Perimeter^2$. This
614 circularity metric provides insight into the roundness of the mesh, where a value closer to 1
615 indicates a shape that is more circular, and values closer to 0 reflect more elongated or irregular
616 shapes. Additionally, the maximum width is defined by identifying the two farthest points along
617 the convex hull boundary and then calculating the greatest perpendicular distance from this line
618 (connecting the farthest points) to any point within the convex hull. This measurement represents
619 the maximum width of the pericyte mesh by assuming its length is the axis with the greater size.
620 In addition, the number of pericyte branches was calculated manually by counting the number of
621 branches on each 3D rendered pericyte.

622 **Quantification of secreted proteins by Luminex Assay**:

623 Secreted protein concentrations were measured from supernatants taken from the outlets of 3D
624 brain microvessels with a 13 x 13 grid geometry. Supernatants from 2-3 devices exposed to the
625 same condition were pooled, diluted 2X and assayed using a 10-plex Human Luminex Discovery
626 Assay from R&D Systems on a Luminex 100/200. The 10-plex panel included: Ang-1, Ang-2,
627 PDGF-BB, N-cadherin, TIMP-1, ANGPTL4, VEGF, Tie-2, IL-8, and CXCL-1. Protein
628 concentrations were interpolated from a 11-point standard curve of known concentrations of
629 recombinant human proteins provided by the vendor and reported as pg/mL using xPONENT 4.2.
630 7 out of 10 analytes were in the standard curve quantification range for 100% of measurements
631 recorded, with Timp-1, N-cadherin and IL-8 having 100% of measurements above the upper limit
632 of quantification.

633 **Measuring changes in barrier integrity by xCELLigence**:

634 xCELLigence 96 well PET E-plates (300600910, Agilent) were coated with 15 µg/mL Poly-L-lysine
635 and 5000 HBMECs in 200 µL EGM-2MV were added per well. After cell adherence, the plate was
636 placed into the xCELLigence RTCA SP reader to begin baseline measurement of growth-related
637 changes in cell index (an arbitrary measure of impedance) and the cells were incubated for 3 days
638 until cell index reached a plateau (indicative of cell confluence). Media was changed every two
639 days. For initial testing of the impact of iRBC-egress media on barrier integrity, on the day of the
640 experiment iRBC-egress media was added at concentrations of either 12.5, 25 or 50 million
641 ruptured iRBC/mL. Changes in cell index were measured every 15-seconds for 8 hours and then
642 every 15-minutes for 48-hours. To test the impact of Ang-1 on *P. falciparum*-iRBC-egress media
643 mediated barrier breakdown, iRBC-egress media was added at $50x10^6$ ruptured iRBC/mL after
644 either a 1- or 18-hour pre-incubation with 1 µg/mL of rAng-1. Again, changes in cell index were

645 measured every 15 seconds for 8 hours and then every 15-minutes for 48-hours. Quantification
646 of partial protection was done by first normalizing each condition to the media only control. Then
647 the area under the curve of the negative values, indicative of barrier breakdown, was calculated
648 using GraphPad Prism (version 10.0.2) where the media only without rAng-1 condition
649 represented an average value of 0 and the iRBC-egress media without rAng-1 condition an
650 average value of 100.

651 **Statistical analysis**:

652 All statistics were obtained by use of GraphPad Prism (version 10.0.2). Non-parametric Mann-
653 Whitney U tests were performed for most experiments, except to calculate Ang-1 protection in the
654 2D xCELLigence experiment in which a repeated measures one-way ANOVA test with Dunnett's
655 multiple comparisons test was performed. A P-value<0.05 was considered statistically significant.

656 **Author contributions.**

657 R.L and M.B conceived the work. R.L, P.R, R.A, and M.B designed experiments. R.L performed
658 most experiments with assistance of F.K, P.R, H.F, M.M, and R.A. R.L, P.R, H.F, W.M, R.A, Y.S,
659 G.M, M.B analyzed the data. R.L and M.B wrote the original draft of the manuscript. All authors
660 contributed to manuscript writing, revision, editing and suggestions.

661 **Acknowledgements**

662 We want to thank Kristina Haase (EMBL Barcelona) for her support and careful suggestions on
663 the project and manuscript writing, as well as for assistance with the generation of mCherry HBVP
664 with help from Violeta Beltran-Sastre. We acknowledge access to the CRG/UPF flow cytometry
665 facility for mCherry HBVP sorting. We are grateful to Carlota Dobaño (ISGlobal) for access to the
666 Luminex and to Michael Blackman (The Francis Crick Institute) who kindly gifted compound 2.
667 This work was facilitated by the EMBL Electron Microscopy Core Facility (EMCF), with important
668 assistance from Viola Oorschot on sample preparation and processing, and Karel Mocaer and
669 Martin Schorb on image analysis. The great majority of this work was supported by the core
670 program funding of the European Molecular Biology Laboratory (EMBL) and the European
671 Research Council (ERC) under the European Union's Horizon 2020 research and innovation
672 program (Grant agreement no. 948088). F.K is funded through the Marie Skłodowska-Curie grant
673 agreement (101068552). H.F is supported by a fellowship from the EMBL Interdisciplinary
674 (EI4POD) program under Marie Skłodowska-Curie Actions COFUND (847543). G.M. is supported
675 by RYC 2020–029886 I/ AEI/10.13039/501100011033, co funded by European Social Fund

676 (ESF). ISGlobal received support from the grant CEX2018-000806-S funded by MCIN/AEI/
677 10.13039/501100011033, and support from the Generalitat de Catalunya through the CERCA
678 Program. This research is part of the ISGlobal's Program on the Molecular Mechanisms of Malaria
679 which is partially supported by the Fundación Ramón Areces.

680

681 **Bibliography:**

682 1. A. M. Dondorp, *et al.*, Artesunate versus quinine in the treatment of severe falciparum
683 malaria in African children (AQUAMAT): an open-label, randomised trial. *The Lancet* **376**, 1647–
684 1657, (2010).

685 2. G. L. Birbeck, *et al.*, Blantyre Malaria Project Epilepsy Study (BMPES) of neurological
686 outcomes in retinopathy-positive paediatric cerebral malaria survivors: a prospective cohort
687 study. *The Lancet Neurology* **9**, 1173–1181, (2010).

688 3. S. Mohanty, *et al.*, Magnetic Resonance Imaging of Cerebral Malaria Patients Reveals
689 Distinct Pathogenetic Processes in Different Parts of the Brain. *mSphere* **2**,
690 10.1128/msphere.00193-17, (2017).

691 4. K. Dorovini-Zis, *et al.*, The Neuropathology of Fatal Cerebral Malaria in Malawian
692 Children. *The American Journal of Pathology* **178**, 2146–2158, (2011).

693 5. A. Kessler, *et al.*, Linking EPCR-Binding PfEMP1 to Brain Swelling in Pediatric Cerebral
694 Malaria. *Cell Host & Microbe* **22**, 601-614.e5, (2017).

695 6. J. Storm, *et al.*, Cerebral malaria is associated with differential cytoadherence to brain
696 endothelial cells. *EMBO Molecular Medicine* **11**, e9164, (2019).

697 7. P. K. Sahu, *et al.*, Determinants of brain swelling in pediatric and adult cerebral malaria.
698 *JCI Insight* **6**, (2022).

699 8. M. Bernabeu, J. D. Smith, EPCR and Malaria Severity: The Center of a Perfect Storm.
700 *Trends in Parasitology* **33**, 295–308, (2017).

701 9. S. C. Wassmer, T. F. de Koning-Ward, G. E. R. Grau, S. Pai, Unravelling mysteries at
702 the perivascular space: a new rationale for cerebral malaria pathogenesis. *Trends in*
703 *Parasitology* **40**, 28–44, (2024).

704 10. H. G. Augustin, G. Young Koh, G. Thurston, K. Alitalo, Control of vascular
705 morphogenesis and homeostasis through the angiopoietin–Tie system. *Nat Rev Mol Cell Biol*
706 **10**, 165–177, (2009).

707 11. S. Fukuhara, *et al.*, Differential function of Tie2 at cell–cell contacts and cell–substratum
708 contacts regulated by angiopoietin-1. *Nat Cell Biol* **10**, 513–526, (2008).

709 12. P. Saharinen, *et al.*, Angiopoietins assemble distinct Tie2 signalling complexes in
710 endothelial cell–cell and cell–matrix contacts. *Nat Cell Biol* **10**, 527–537, (2008).

711 13. M. R. Siddiqui, C. S. Mayanil, K. S. Kim, T. Tomita, Angiopoietin-1 Regulates Brain
712 Endothelial Permeability through PTPN-2 Mediated Tyrosine Dephosphorylation of Occludin.
713 *PLOS ONE* **10**, e0130857, (2015).

714 14. P. C. Maisonpierre, *et al.*, Angiopoietin-2, a Natural Antagonist for Tie2 That Disrupts in
715 vivo Angiogenesis. *Science* **277**, 55–60, (1997).

716 15. S. Gurnik, *et al.*, Angiopoietin-2-induced blood–brain barrier compromise and increased
717 stroke size are rescued by VE-PTP-dependent restoration of Tie2 signaling. *Acta Neuropathol*
718 **131**, 753–773, (2016).

719 16. J. Golledge, *et al.*, Plasma Angiopoietin-1 Is Lower After Ischemic Stroke and
720 Associated With Major Disability But Not Stroke Incidence. *Stroke* **45**, 1064–1068, (2014).

721 17. T. W. Yeo, *et al.*, Angiopoietin-2 is associated with decreased endothelial nitric oxide
722 and poor clinical outcome in severe falciparum malaria. *Proceedings of the National Academy of*
723 *Sciences* **105**, 17097–17102, (2008).

724 18. F. E. Lovegrove, *et al.*, Serum Angiopoietin-1 and -2 Levels Discriminate Cerebral
725 Malaria from Uncomplicated Malaria and Predict Clinical Outcome in African Children. *PLOS*
726 *ONE* **4**, e4912, (2009).

727 19. A. L. Conroy, *et al.*, Whole blood angiopoietin-1 and -2 levels discriminate cerebral and
728 severe (non-cerebral) malaria from uncomplicated malaria. *Malaria Journal* **8**, 295, (2009).

729 20. A. L. Conroy, *et al.*, Angiopoietin-2 levels are associated with retinopathy and predict
730 mortality in Malawian children with cerebral malaria: A retrospective case–control study*. *Critical*
731 *Care Medicine* **40**, 952, (2012).

732 21. V. Jain, *et al.*, Plasma levels of angiopoietin-1 and -2 predict cerebral malaria outcome in
733 Central India. *Malar J* **10**, 383, (2011).

734 22. C. Gomes, *et al.*, Endothelial transcriptomic analysis identifies biomarkers of severe and
735 cerebral malaria. *JCI Insight* **8**, (2023).

736 23. U. Fiedler, *et al.*, The Tie-2 ligand Angiopoietin-2 is stored in and rapidly released upon
737 stimulation from endothelial cell Weibel-Palade bodies. *Blood* **103**, 4150–4156, (2004).

738 24. S. Ornelas, *et al.*, Three-dimensional ultrastructure of the brain pericyte-endothelial
739 interface. *J Cereb Blood Flow Metab* **41**, 2185–2200, (2021).

740 25. R. Daneman, A. Prat, The Blood–Brain Barrier. *Cold Spring Harb Perspect Biol* **7**,
741 a020412, (2015).

742 26. F. Fernández-Klett, *et al.*, Early Loss of Pericytes and Perivascular Stromal Cell-Induced
743 Scar Formation after Stroke. *J Cereb Blood Flow Metab* **33**, 428–439, (2013).

744 27. J. D. Sengillo, *et al.*, Deficiency in Mural Vascular Cells Coincides with Blood–Brain
745 Barrier Disruption in Alzheimer's Disease. *Brain Pathology* **23**, 303–310, (2013).

746 28. A. P. Sagare, *et al.*, Pericyte loss influences Alzheimer-like neurodegeneration in mice.
747 *Nat Commun* **4**, 2932, (2013).

748 29. V. Barrera, *et al.*, Neurovascular sequestration in paediatric P. falciparum malaria is
749 visible clinically in the retina. *eLife* **7**, e32208, (2018).

750 30. K. Haase, M. R. Gillrie, C. Hajal, R. D. Kamm, Pericytes Contribute to Dysfunction in a
751 Human 3D Model of Placental Microvasculature through VEGF-Ang-Tie2 Signaling. *Advanced*
752 *Science* **6**, 1900878, (2019).

753 31. M. Bernabeu, *et al.*, Binding Heterogeneity of Plasmodium falciparum to Engineered 3D
754 Brain Microvessels Is Mediated by EPCR and ICAM-1. *mBio* **10**, e00420-19, (2019).

755 32. C. Howard, F. Joof, R. Hu, J. D. Smith, Y. Zheng, Probing cerebral malaria inflammation
756 in 3D human brain microvessels. *Cell Reports* **42**, 113253, (2023).

757 33. Y. Zheng, *et al.*, In vitro microvessels for the study of angiogenesis and thrombosis.
758 *Proceedings of the National Academy of Sciences* **109**, 9342–9347, (2012).

759 34. T. M. Mathiisen, K. P. Lehre, N. C. Danbolt, O. P. Ottersen, The perivascular astroglial
760 sheath provides a complete covering of the brain microvessels: An electron microscopic 3D
761 reconstruction. *Glia* **58**, 1094–1103, (2010).

762 35. M. T. Uemura, T. Maki, M. Ihara, V. M. Y. Lee, J. Q. Trojanowski, Brain Microvascular
763 Pericytes in Vascular Cognitive Impairment and Dementia. *Front. Aging Neurosci.* **12**, (2020).

764 36. L. He, *et al.*, Analysis of the brain mural cell transcriptome. *Sci Rep* **6**, 35108, (2016).

765 37. D. Attwell, A. Mishra, C. N. Hall, F. M. O'Farrell, T. Dalkara, What is a pericyte? *J Cereb*
766 *Blood Flow Metab* **36**, 451–455, (2016).

767 38. F. Oliveira, O. Bondareva, J. R. Rodríguez-Aguilera, B. N. Sheikh, Cultured brain
768 pericytes adopt an immature phenotype and require endothelial cells for expression of canonical
769 markers and ECM genes. *Front. Cell. Neurosci.* **17**, (2023).

770 39. W. Denk, H. Horstmann, Serial Block-Face Scanning Electron Microscopy to
771 Reconstruct Three-Dimensional Tissue Nanostructure. *PLOS Biology* **2**, e329, (2004).

772 40. C. J. Peddie, *et al.*, Volume electron microscopy. *Nat Rev Methods Primers* **2**, 51,
773 (2022).

774 41. P. C. Nahirney, P. Reeson, C. E. Brown, Ultrastructural analysis of blood–brain barrier
775 breakdown in the peri-infarct zone in young adult and aged mice. *J Cereb Blood Flow Metab* **36**,
776 413–425, (2016).

777 42. L. C. D. Smyth, *et al.*, Markers for human brain pericytes and smooth muscle cells.
778 *Journal of Chemical Neuroanatomy* **92**, 48–60, (2018).

779 43. R. I. Grant, *et al.*, Organizational hierarchy and structural diversity of microvascular
780 pericytes in adult mouse cortex. *J Cereb Blood Flow Metab* **39**, 411–425, (2019).

781 44. M. R. Gillrie, *et al.*, Src-family kinase–dependent disruption of endothelial barrier function
782 by Plasmodium falciparum merozoite proteins. *Blood* **110**, 3426–3435, (2007).

783 45. J. Gallego-Delgado, *et al.*, Angiotensin receptors and β-catenin regulate brain
784 endothelial integrity in malaria. *Journal of Clinical Investigation* **126**, 4016–4029, (2016).

785 46. P. Pal, *et al.*, Plasmodium falciparum Histidine-Rich Protein II Compromises Brain
786 Endothelial Barriers and May Promote Cerebral Malaria Pathogenesis. *mBio* **7**,
787 10.1128/mbio.00617-16, (2016).

788 47. J. Storm, Y. Wu, J. Davies, C. A. Moxon, A. G. Craig, Testing the effect of PAR1
789 inhibitors on Plasmodium falciparum-induced loss of endothelial cell barrier function. *Wellcome*
790 *Open Res* **5**, 34, (2020).

791 48. C. A. Moxon, *et al.*, Parasite histones are toxic to brain endothelium and link blood
792 barrier breakdown and thrombosis in cerebral malaria. *Blood Adv* **4**, 2851–2864, (2020).

793 49. S. J. Higgins, *et al.*, Dysregulation of angiopoietin-1 plays a mechanistic role in the
794 pathogenesis of cerebral malaria. *Sci Transl Med* **8**, 358ra128, (2016).

795 50. V. Tran, *et al.*, The Angiopoietin-Tie2 axis contributes to placental vascular disruption
796 and adverse birth outcomes in malaria in pregnancy. *eBioMedicine* **73**, (2021).

797 51. M. Zuniga, *et al.*, Plasmodium falciparum and TNF-α Differentially Regulate
798 Inflammatory and Barrier Integrity Pathways in Human Brain Endothelial Cells. *mBio* **13**,
799 e01746-22, (2022).

800 52. A. Armulik, *et al.*, Pericytes regulate the blood–brain barrier. *Nature* **468**, 557–561,
801 (2010).

802 53. E. Pongponratn, *et al.*, An ultrastructural study of the brain in fatal Plasmodium
803 falciparum malaria. *Am J Trop Med Hyg* **69**, 345–359, (2003).

804 54. G. M. de Jong, J. J. Slager, A. Verbon, J. J. van Hellemond, P. J. J. van Genderen,
805 Systematic review of the role of angiopoietin-1 and angiopoietin-2 in Plasmodium species
806 infections: biomarkers or therapeutic targets? *Malaria Journal* **15**, 581, (2016).

807 55. A. L. Conroy, *et al.*, Endothelium-Based Biomarkers Are Associated with Cerebral
808 Malaria in Malawian Children: A Retrospective Case-Control Study. *PLOS ONE* **5**, e15291,
809 (2010).

810 56. R. L. Nachman, S. Rafii, Platelets, Petechiae, and Preservation of the Vascular Wall.
811 *New England Journal of Medicine* **359**, 1261–1270, (2008).

812 57. P. Saharinen, L. Eklund, K. Alitalo, Therapeutic targeting of the angiopoietin-TIE
813 pathway. *Nat Rev Drug Discov* **16**, 635–661, (2017).

814 58. J. Hanson, *et al.*, Microvascular obstruction and endothelial activation are independently
815 associated with the clinical manifestations of severe falciparum malaria in adults: an
816 observational study. *BMC Medicine* **13**, 122, (2015).

817 59. P. Prapansilp, *et al.*, A clinicopathological correlation of the expression of the
818 angiopoietin-Tie-2 receptor pathway in the brain of adults with Plasmodium falciparum malaria.
819 *Malaria Journal* **12**, 50, (2013).

820 60. P. Pichiule, J. C. Chavez, J. C. LaManna, Hypoxic Regulation of Angiopoietin-2
821 Expression in Endothelial Cells*. *Journal of Biological Chemistry* **279**, 12171–12180, (2004).

822 61. C. Sundberg, M. Kowanetz, L. F. Brown, M. Detmar, H. F. Dvorak, Stable Expression of
823 Angiopoietin-1 and Other Markers by Cultured Pericytes: Phenotypic Similarities to a
824 Subpopulation of Cells in Maturing Vessels During Later Stages of Angiogenesis *In Vivo*.
825 *Laboratory Investigation* **82**, 387–401, (2002).

826 62. T. Nishishita, P. C. Lin, Angiopoietin 1, PDGF-B, and TGF-β gene regulation in
827 endothelial cell and smooth muscle cell interaction. *Journal of Cellular Biochemistry* **91**, 584–
828 593, (2004).

829 63. X. Wei, S. Jessa, C. L. Kleinman, T. N. Phoenix, Mapping Angiopoietin1 Expression in
830 the Developing and Adult Brain. *Developmental Neuroscience* **43**, 321–334, (2021).

831 64. L. Piatti, C. C. Howard, Y. Zheng, M. Bernabeu, "Binding of Plasmodium falciparum-
832 Infected Red Blood Cells to Engineered 3D Microvessels" in *Malaria Immunology*, Methods in
833 Molecular Biology., A. T. R. Jensen, L. Hviid, Eds. (Springer US, 2022), , pp. 557–585.

834 65. B. Titze, C. Genoud, R. W. Friedrich, SBEMimage: Versatile Acquisition Control
835 Software for Serial Block-Face Electron Microscopy. *Front. Neural Circuits* **12**, (2018).

836 66. G. Mahalingam, *et al.*, A scalable and modular automated pipeline for stitching of large
837 electron microscopy datasets. *eLife* **11**, e76534, (2022).

838 67. waleedmirzaPhD, waleedmirzaPhD/cell_analysis_toolkit, (2024), . Deposited February
839 24, 2024.

840 68. P. Virtanen, *et al.*, SciPy 1.0: fundamental algorithms for scientific computing in Python.
841 *Nat Methods* **17**, 261–272, (2020).

842

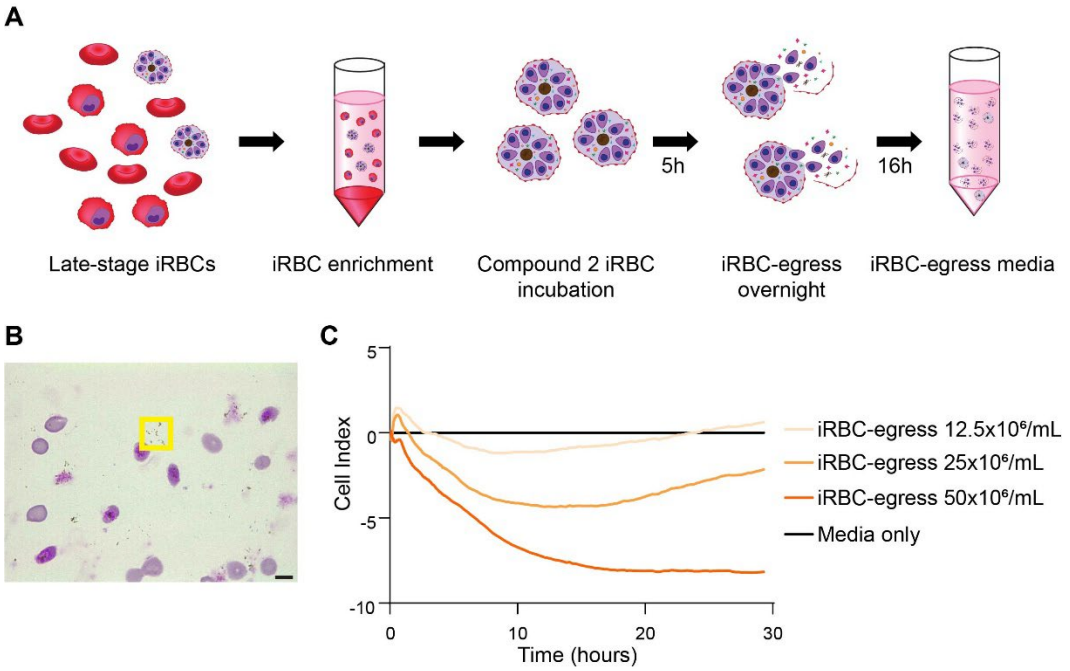

843

Fig. S1. Preparation of iRBC-egress media that induces barrier breakdown. *(A)* Schematic representation of the protocol to make iRBC-egress media. In short, late-stage *P. falciparum*-iRBC are purified by a gelaspan gradient separation and then incubated for 5 hours with compound-2 to synchronize them at the point of egress. Compound-2 is removed and the *P. falciparum*-iRBC are resuspended in vascular growth media and left overnight on a shaker at 50 rpm to egress. *(B)* A thin smear taken from the resultant iRBC-egress media before centrifugation stained with giemsa. The yellow box highlights free hemozoin particles. Scale bar represents 5 µm. *(C)* Representative recording data of xCELLigence measurements on 2D HBMEC monolayers in the absence of HBVP taken after addition of iRBC-egress media at different concentrations. Data is normalized to the media-only control.

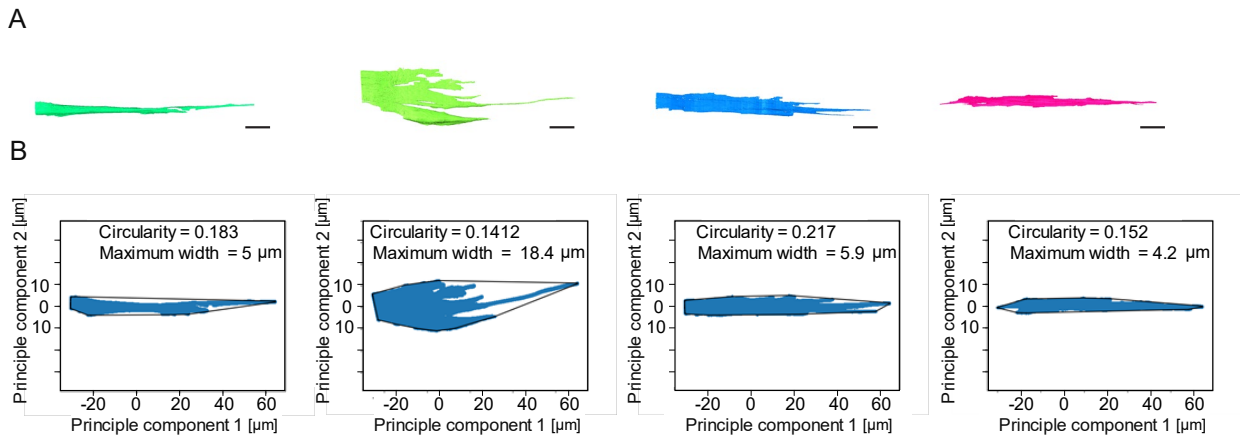

Fig. S2. Morphology analysis of segmented pericytes from SBF-SEM. *(A)* The analysis pipeline begins with the extraction of 3D segmented pericyte meshes. Shown here are four representative pericytes. *(B)* Pericyte geometry is flattened into two principal dimensions using PCA by a Python-based image analysis pipeline. The 2D geometry's shape is then determined using convex hull analysis. To describe pericyte morphology, pericyte cell borders are analyzed for circularity, calculated as 4π*Area/Perimeter^2, where a value of 1 indicates a perfect circle and values approaching 0 indicate increasingly elongated shapes, and maximum width.

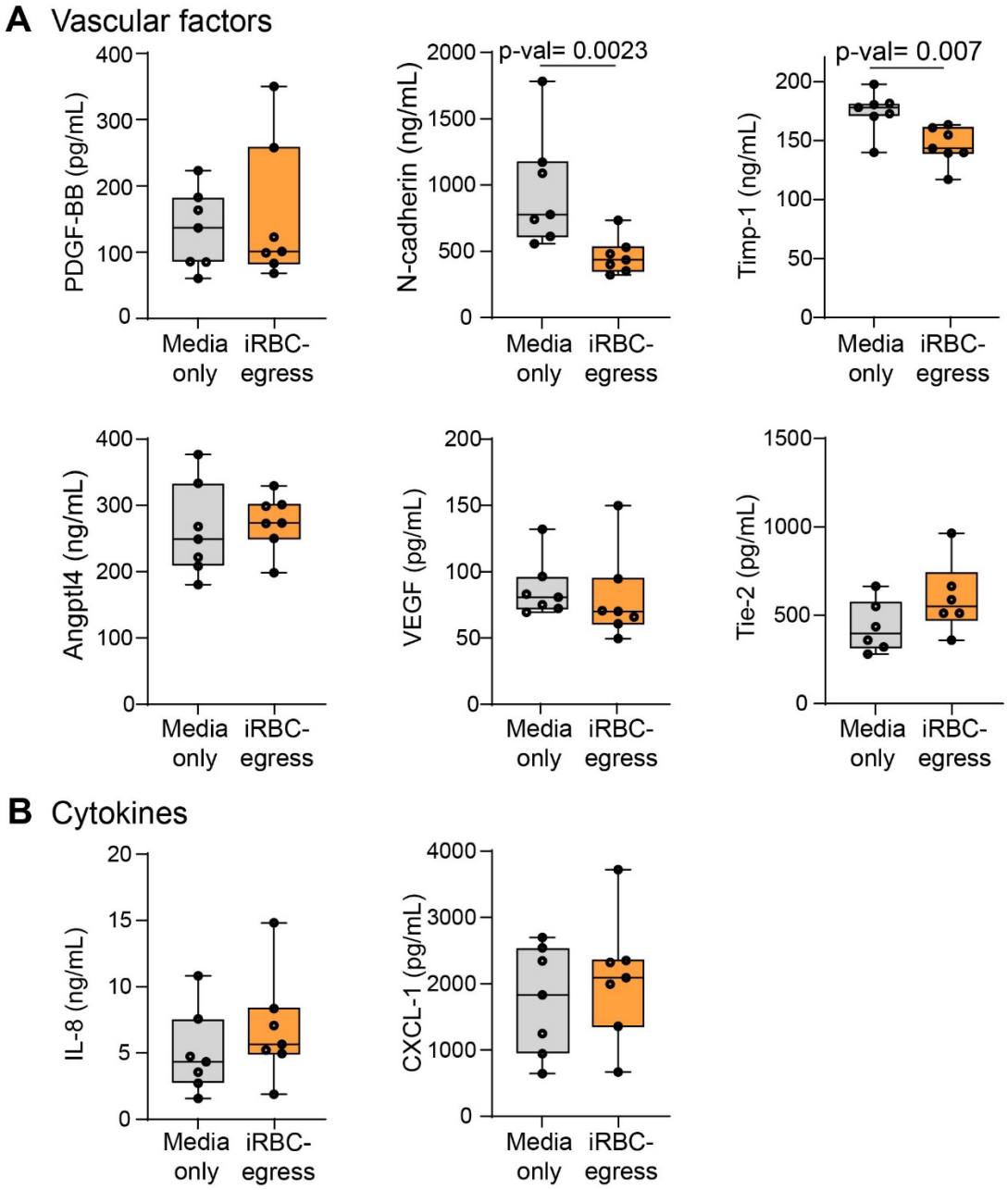

Fig. S3. Changes in secreted vascular factors and cytokines following iRBC-egress media incubation. *(A)* Concentrations of vascular factors PDGF-BB, N-cadherin, Timp-1, Angptl4, VEGF and Tie-2 measured by Luminex from 3D brain microvessels supernatants treated with media only or iRBC-egress media for 18-hours. *(B)* Concentrations of released cytokines IL-8 and CXCL-1 measured by Luminex from 3D brain microvessels supernatants treated with media only or iRBC-egress media for 18-hours. Box and whisker plots display the median, 25th and 75th percentiles and the minimum and maximum data points in A and B. Data points represent supernatants pooled from 2-3 devices in 6-7 independent experiments. Statistical significance is analyzed by Mann-Whitney U test.

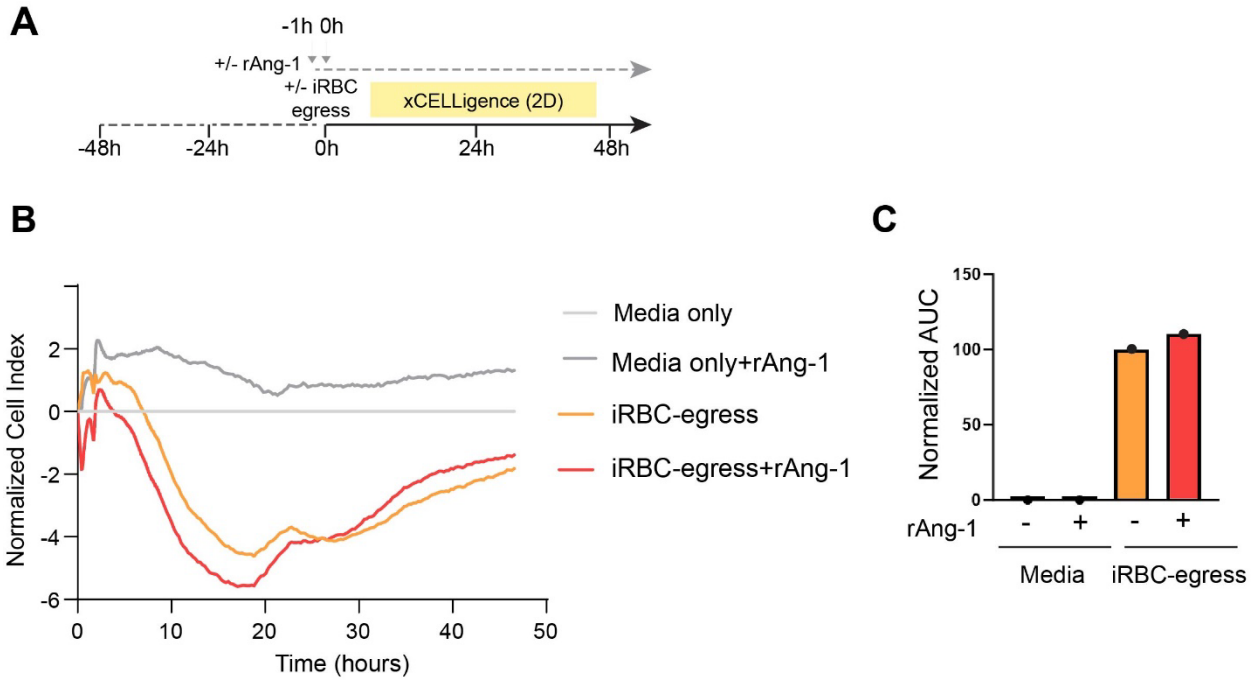

876

877 **Fig. S4.** Short time pre-incubations with rAng-1 does not protect against increased permeability
878 induced by iRBC-egress media. (A) Experimental outline of short-term (1-hour) incubation with
879 rAng-1 in a 2DHBMEC monolayer in the absence of HBVP. (B) Representative recording data of
880 xCELLigence measurements taken after +/- addition of rAng-1. All conditions were normalized to
881 the media only control. (C) Area under the curve analysis. All conditions were normalized to *P.*
882 *falciparum*-iRBC-egress media as 100. Data points represent 1 independent experiment run in
883 triplicate.

884